A New Dynamic Minimal Path Model for Tubular Structure Centerline Delineation

Da Chen[1,2] and Laurent D. Cohen[1]
[1]University Paris Dauphine, PSL Research University, CNRS, UMR 7534, CEREMADE, 75016 Paris, France
[2]Centre Hospitalier National d'Ophtalmologie des Quinze-Vingts, Paris, France
Email: {chenda, cohen}@ceremade.dauphine.fr

***Abstract*—We propose a new dynamic Riemannian metric with adaptive anisotropy enhancement and with appearance feature coherence penalization. The appearance features are characterized by the orientation score maps. Unlike the static geodesic metrics which depend on local pointwise information, the dynamic metric can take into account the nonlocal feature coherence penalty in order to extract a desired structure from complicated background or from a vessel tree. We construct the metric using the information from two external reference points which are identified during the geodesic distance computation. Numerical experiments are performed in retinal vessels, including the independent results from the proposed dynamic metric itself and the comparison against existing minimal path models. The results show that the proposed metric indeed gets better performance than state-of-the-art geodesic metrics.**

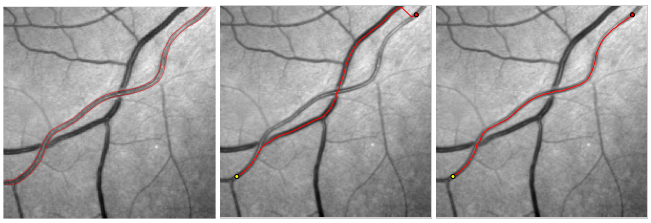

(a) (b) (c)

Fig. 1. Short branches combination problem. **a** Original image with boundaries of target vessel. **b** Minimal path from the anisotropic Riemannian metric [6]. **c** Minimal path from the proposed dynamic metric.

I. Introduction

The minimal path model [1] is a robust and efficient method for vessel extraction. In its basic formulation, a tubular structure can be naturally modelled as a minimal path. It seeks a globally optimal curve that minimizes the path length

$$\mathcal{L}(\gamma) = \int_0^1 P(\gamma(t))\|\gamma'(t)\|dt$$

along a path γ with Lipschitz continuity, where s is the arc-length parameter of γ such that $\|\gamma'(s)\| \equiv 1$ and P is a potential function with small values inside the tubular structure. The minimal path model is able to efficiently find the global optimality of the path length $\mathcal{L}$ through the solution to the Eikonal partial differential equation (PDE) thanks to the well-established numerical solvers like the fast marching methods [2], [3]. By designing suitable potentials P, the minimal path model can be applied to solve various vessel segmentation problems [4].

One of the key ingredients for the minimal path computation is the used geodesic metrics. In order to address various tubular structure segmentation problems, a series of geodesic metrics have been designed. The Li-Yezzi minimal path model [5] defined an isotropic Riemannian metric in a multi-scale space to solve the problem of simultaneously finding the vessel centerlines and boundaries. Benmansour and Cohen [6] generalized the Li-Yezzi model to the anisotropic Riemannian case, where the vessel orientations were also used to mitigate the shortcuts problem. Péchaud *et al.* [7] added an abstract orientation dimension to the multi-scale space, which provides an orientation-lifted way to use the tubular orientation information. The elastica geodesic metrics [8] and the Reeds-Sheep metrics [9], [10] can be used to minimize the path length with second-order regularization term such as the curvatures. These metrics have beed successfully applied to retinal imaging. In [11], a new minimal path extraction method in conjunction with a fast marching front frozen scheme was proposed. The path features like curvatures are estimated through the truncated geodesics from the front points, which will be frozen if their path features do not satisfy the prescribed criteria. The idea of using truncated geodesics to estimate the features are also used in this paper. In order to reduce the user intervention, the keypoints methods [12]–[14] iteratively add new source points in the course of geodesic distance computation. The approaches listed above are not exhaustive and other interesting methods relevant to minimal path-based tubularity segmentation include [15], [16].

In this paper, we propose a new dynamic geodesic metric for tubular centerline delineation. The main contribution lies at the construction of a metric with adaptive anisotropy enhancement and feature coherence penalty in a dynamic manner. The computation of the dynamic metric is carried out during the fast marching fronts propagation in conjunction with a truncated geodesics tracking scheme. The new dynamic metric is able to reduce the risk of tracking incorrect tubular structures. In Fig. 1b, we show a typical short combination problem suffered by the anisotropic Riemannian metric [6]. In Fig. 1c, we illustrate the result from the proposed metric which avoids this problem.

The paper is organized as follows. In Section II, we briefly introduce the computation of the tubular features. In Sec-

tion III, we introduce the construction method for the dynamic metric. The experimental results are presented in Section V.

II. Local Tubularity Descriptor

We suppose that the gray levels inside the tubular structures are *locally darker* than the background. A tubular structure or a vessel can be described by a feature vector field and by a vesselness map. The feature vector field indicates the vessel orientation at each point and the vesselness map indicates the probability of a point belonging to a vessel. Both maps can be detected through any multi-scale steerable filters such as [17], [18]. In this paper, we choose the optimally oriented flux (OOF) filter, as our vessel detector. It invokes a Gaussian filter G_σ with variance σ and a characteristic function χ_r of a disk with radius r

$$\mathbf{OF}(\mathbf{x}, r) := \frac{1}{r}\begin{pmatrix} \partial_{xx}G_\sigma & \partial_{xy}G_\sigma \\ \partial_{yx}G_\sigma & \partial_{y}G_\sigma \end{pmatrix} * \chi_r(\mathbf{x}) * I(\mathbf{x}), \quad (1)$$

where $\partial_{xy}G_\sigma$ is the second-order derivative of G_σ and $I : \Omega \to \mathbb{R}$ is a gray level image. For each point $\mathbf{x}$ and scale r, the OOF response $\mathbf{OF}(\mathbf{x}, r)$ is a 2×2 symmetric matrix with eigenvalues $\hat{\varrho}_1(\mathbf{x}, r)$ and $\hat{\varrho}_2(\mathbf{x}, r)$. Let $\hat{\mathfrak{q}}_{\rm of}(\mathbf{x}, r)$ be the eigenvector corresponding to the eigenvalue $\hat{\varrho}_2(\mathbf{x}, r)$. Without loss of generality, we assume that $\hat{\varrho}_1(\mathbf{x}, r) \le \hat{\varrho}_2(\mathbf{x}, r)$ and if $\hat{\mathbf{x}}$ is inside a vessel one further has $\hat{\varrho}_1(\mathbf{x}, r) \approx 0$. At each point $\mathbf{x}$, one can define an optimal scale

$$\zeta(\mathbf{x}) = \arg\max_r \ \hat{\varrho}_2(\mathbf{x}, r).$$

Let $\mathbb{S}^1 = [0, 2\pi)$ be an orientation space with periodic boundary condition and let $\mathfrak{g}(\theta) = (\cos\theta, \sin\theta)^T$ be an unit vector associated to an angle $\theta \in \mathbb{S}^1$. An orientation score (OS) map $\psi_{\rm os} : \Omega \times \mathbb{S}^1 \to \mathbb{R}$ can be computed by

$$\psi_{\rm os}(\mathbf{x}, \theta) = \max\{\langle \mathfrak{g}^\perp(\theta), \mathbf{OF}(\mathbf{x}, \zeta(\mathbf{x}))\mathfrak{g}^\perp(\theta)\rangle, 0\}, \quad (2)$$

with $\mathfrak{g}^\perp(\theta) = (-\sin\theta, \cos\theta)^T$ a vector orthogonal to $\mathfrak{g}(\theta)$.

A feature map $\mathfrak{q}_{\rm of}$ is defined by

$$\mathfrak{q}_{\rm of}(\mathbf{x}) = \hat{\mathfrak{q}}_{\rm of}(\mathbf{x}, \zeta(\mathbf{x})). \quad (3)$$

III. Dynamic Metric with Coherence Penalization and Adaptive Anisotropy Enhancement

A. Potentially Asymmetric Orientation Score

We consider an oriented Gaussian kernel $Q^\theta_{\underline{\sigma}}$ associated to $\theta \in \mathbb{S}^1$ which can be expressed for any $\mathbf{x} \in \Omega$ by

$$Q^\theta_{\underline{\sigma}}(\mathbf{x}) = \exp\left(-\frac{|\langle \mathfrak{g}(\theta), \mathbf{x}\rangle|^2}{2\sigma_1^2} - \frac{|\langle \mathfrak{g}^\perp(\theta), \mathbf{x}\rangle|^2}{2\sigma_2^2}\right),$$

where $\underline{\sigma} = (\sigma_1, \sigma_2)$ with σ_1 and σ_2 ($\sigma_1 \gg \sigma_2$) being the Gaussian variances along the directions $\mathfrak{g}_\theta$ and $\mathfrak{g}^\perp_\theta$, respectively. Here we further consider an asymmetric Gaussian kernel through a cutoff function $\delta^\theta : \Omega \to \{0, 1\}$

$$\delta^\theta(\mathbf{x}) = \begin{cases} 1, & \text{if } \langle \nabla G_{\sigma_1}(\mathbf{x}),\ \mathfrak{g}(\theta)\rangle \ge \epsilon_0, \\ 0, & \text{otherwise,} \end{cases}$$

where $\nabla G_{\sigma_1} = (\partial_x G_{\sigma_1}, \partial_y G_{\sigma_1})^T$ is the standard Euclidean gradient of the isotropic Gaussian kernel G_{σ_1} with variance σ and $\epsilon_0 \in \mathbb{R}^+_0$ is a sufficiently small constant. An asymmetric Gaussian kernel $\mathcal{H}^\theta_{\underline{\sigma}}$ over the domain Ω can be expressed by

$$\mathcal{H}^\theta_{\underline{\sigma}}(\mathbf{x}) = \delta^\theta(\mathbf{x})\, Q^\theta_{\underline{\sigma}}(\mathbf{x}).$$

A new potentially asymmetric OS map $\Psi_{\rm os}$ for each *fixed* orientation $\theta \in \mathbb{S}^1$ is defined by

$$\Psi_{\rm os}(\mathbf{x}, \theta) = \frac{(\mathcal{H}^{\pi+\theta}_{\underline{\sigma}} * \psi^\theta_{\rm os})(\mathbf{x})}{\int_\Omega \mathcal{H}^{\pi+\theta}_{\underline{\sigma}}(\mathbf{x})\, d\mathbf{x}}, \quad \psi^\theta_{\rm os}(\cdot) := \frac{\psi_{\rm os}(\cdot, \theta)}{\|\psi_{\rm os}\|_\infty}, \quad (4)$$

where $*$ is a convolution operator.

B. Crossing-adaptive Tensor Field

In an image which involves tubular tree structures, there may exist a set of points belonging to different vessels. These points are crossing points, for which one needs more than one orientation vectors to describe the tubular anisotropic property. In this case, it may increase the risk of obtaining incorrect geodesic tangents at these crossing points. A possible solution is to design a crossing-adaptive Riemannian metric, which should be weakly anisotropic (or approximately isotropic) at these crossing points but be strongly anisotropic at the other points inside the tubular tree. This can be done by taking into account the orientation score values at the crossing points to establish the relevant tensor field [19]. In contrast to [19] which uses the score values corresponding to all the orientations, in this section we only consider the score values with respect to locally optimal orientations. For this purpose, we first define a set $\mathfrak{M}_{\mathbf{x}}$ involving locally optimal feature vectors in the sense of orientation score map. For each point $\mathbf{x}$, the set $\mathfrak{M}_{\mathbf{x}}$ of locally optimal feature vectors associated to $\Psi_{\rm os}(\mathbf{x}, \cdot)$ can be defined by

$$\mathfrak{M}_{\mathbf{x}} = \Big\{\mathfrak{g}(\theta^*);\ \Psi_{\rm os}(\mathbf{x}, \theta^*) > \Psi_{\rm os}(\mathbf{x}, \theta),\ \forall\theta \in N(\theta^*, \xi), \\ \text{and} \quad \Psi_{\rm os}(\mathbf{x}, \theta^*) > \frac{1}{2\pi}\int_0^{2\pi} \Psi_{\rm os}(\mathbf{x}, \theta)\, d\theta\Big\},$$

where $N(\theta^*, \xi)$ is a neighbourhood of $\theta^* \in \mathbb{S}^1$ with length of ξ. The characteristic function of the set $\mathfrak{M}_{\mathbf{x}}$ is expressed as

$$\mathfrak{C}(\mathbf{x}, \theta) = \begin{cases} 1, & \text{if } \mathfrak{g}(\theta) \in \mathfrak{M}_{\mathbf{x}}, \\ 0, & \text{otherwise.} \end{cases}$$

Similar to $\mathfrak{M}_{\mathbf{x}}$, the set of locally optimal directions associated to $\psi_{\rm os}(\mathbf{x}, \theta)$ is denoted by $\overline{\mathfrak{M}}_{\mathbf{x}},\ \forall\mathbf{x} \in \Omega$.

Let $\mathrm{I_d}$ be the 2×2 identity matrix. A tensor field $T_{\rm base}$ can be constructed by

$$T_{\rm base}(\mathbf{x}) = \frac{\int_0^{2\pi} \mathfrak{C}(\mathbf{x}, \theta)\Psi_{\rm os}(\mathbf{x}, \theta)\mathfrak{g}(\theta)\mathfrak{g}(\theta)^T d\theta}{\max\left\{\int_0^{2\pi} \mathfrak{C}(\mathbf{x}, \theta)d\theta, \epsilon_1\right\}} + \mu_0\, \mathrm{I_d}, \quad (5)$$

where μ_0 and ϵ_1 are sufficiently small positive constants. The matrix $\mu_0\, \mathrm{I_d}$ ensures the non-singularity of the matrix $T_{\rm base}(\mathbf{x}),\ \forall\mathbf{x} \in \Omega$.

The desired tensor field $T_{\rm os} : \Omega \to S^+_2$ for the anisotropy-adaptive Riemannian metric can be computed in terms of $T_{\rm base}$

$$T_{\rm os}(\mathbf{x}) = \exp\left(-\alpha \max_{\theta\in\mathbb{S}^1} \psi_{\rm os}(\mathbf{x}, \theta)\right) T^{-1}_{\rm base}(\mathbf{x}). \quad (6)$$

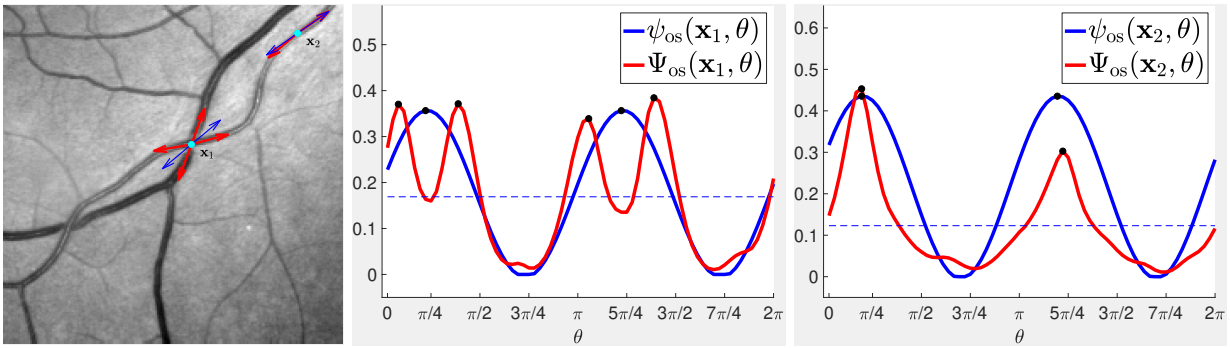

Fig. 2. **Left** The red and blue arrows at point $\mathbf{x}_1$ (resp. $\mathbf{x}_2$) respectively indicate the elements involved in $\mathfrak{M}_{\mathbf{x}_1}$ (resp. $\mathfrak{M}_{\mathbf{x}_2}$) and $\overline{\mathfrak{M}}_{\mathbf{x}_1}$ (resp. $\overline{\mathfrak{M}}_{\mathbf{x}_2}$). **Middle** The red and blue curves respectively indicate the values of $\Psi_{\rm os}(\mathbf{x}_1,\theta)$ and $\psi_{\rm os}(\mathbf{x}_1,\theta)$. Black dots are the peak orientations. **Right** The red and blue curves respectively indicate the values of $\Psi_{\rm os}(\mathbf{x}_2,\theta)$ and $\psi_{\rm os}(\mathbf{x}_2,\theta)$.

where $\alpha \in \mathbb{R}^+$ is a positive constant that controls the contrast ratio and $T_{\rm base}^{-1}(\mathbf{x})$ is the inverse matrix of $T_{\rm base}(\mathbf{x})$.

C. Coherence-Penalized Dynamic Riemannian Metric

Let $\mathfrak{p}:\Omega \to \mathfrak{M}_{\mathbf{x}}$ be a new tubular anisotropy feature map, which corresponds to an orientation map $\mathfrak{a}:\Omega \to \mathbb{S}^1$, where $\mathfrak{a}(\mathbf{x})$ is defined being such that $(\cos(\mathfrak{a}(\mathbf{x})),\sin(\mathfrak{a}(\mathbf{x})))^T = \mathfrak{p}(\mathbf{x})$. At a crossing point $\mathbf{x}$, the feature vector $\mathfrak{p}(\mathbf{x})$ should be proportional to the centerline tangent of the target vessel at $\mathbf{x}$. Let $\mathbf{x}$, $\mathbf{a}_{\mathbf{x}}$, $\mathbf{b}_{\mathbf{x}} \in \Omega$ be three points belonging to the same tubular structure. The points $\mathbf{a}_{\mathbf{x}}$ and $\mathbf{b}_{\mathbf{x}}$, which are named *reference* points, are supposed to be approximately located at the tubular centerline. In addition, we also suppose the point $\mathbf{x}$ is close to the reference point $\mathbf{a}_{\mathbf{x}}$. In the following, we solve the problem for the computation of the coherence penalty at a point $\mathbf{x}$ providing its reference points $\mathbf{a}_{\mathbf{x}}$ and $\mathbf{b}_{\mathbf{x}}$ are known.

The computation criterion for the feature vector $\mathfrak{p}(\mathbf{x})$ is based on the prior that $\mathfrak{p}(\mathbf{a}_{\mathbf{x}})$ and $\mathfrak{p}(\mathbf{b}_{\mathbf{x}})$ have been known. Since $\mathbf{x}$ and $\mathbf{a}_{\mathbf{x}}$ is close to each other, the measurement $|\langle \mathfrak{p}(\mathbf{x}), \mathfrak{p}(\mathbf{a}_{\mathbf{x}})\rangle| \approx 1$ should be held. We define a set $\mathfrak{M}_{\mathbf{x}}^* \subseteq \mathfrak{M}_{\mathbf{x}}$ of the selected feature vectors by

$$\mathfrak{M}_{\mathbf{x}}^* = \{\mathbf{w}^*; \mathbf{w}^* = \arg\max_{\mathbf{w}\in\mathfrak{M}_{\mathbf{x}}} |\langle \mathbf{w}, \mathfrak{p}(\mathbf{a}_{\mathbf{x}})\rangle|\}.$$

Thus the feature vector $\mathfrak{p}(\mathbf{x})$ can be identified by

$$\mathfrak{p}(\mathbf{x}) := (\cos\theta_{\mathbf{x}}^*, \sin\theta_{\mathbf{x}}^*)^T, \tag{7}$$

where the orientation $\theta_{\mathbf{x}}$ is computed by

$$\theta_{\mathbf{x}}^* := \arg\min_{\theta:\mathfrak{g}(\theta)\in\mathfrak{M}_{\mathbf{x}}^*} |\Psi_{\rm os}(\mathbf{x},\theta) - \Psi_{\rm os}(\mathbf{a}_{\mathbf{x}}, \mathfrak{a}(\mathbf{a}_{\mathbf{x}}))|.$$

For a *crossing* point $\mathbf{x}$, each feature vector in $\mathfrak{M}_{\mathbf{x}}$ characterizes the orientation that the tubular structure should have at $\mathbf{x}$ through the map $\mathfrak{a}$. The map $\mathfrak{p}$ is constructed in a progressive way. For the source point $\mathbf{s}$, the feature vector $\mathfrak{p}(\mathbf{s}) = (\cos(\mathfrak{a}(\mathbf{s})),\sin(\mathfrak{a}(\mathbf{s})))^T$ is chosen being such that

$$\mathfrak{a}(\mathbf{s}) = \arg\max_{\theta} \Psi_{\rm os}(\mathbf{s},\theta)$$

The progressive procedure for the computation of $\mathfrak{p}$ and $\mathfrak{a}$ is is detailed in Section IV. Once the feature vector $\mathfrak{p}(\mathbf{x})$ and the corresponding orientation $\mathfrak{a}(\mathbf{x})$ at point $\mathbf{x}$ are detected, we can construct a coherence penalization term which is comprised of two components. The first component is a scalar field $E_{\rm os}$ computed by the enhanced orientation score map $\Psi_{\rm os}$ and the reference point $\mathbf{b}_{\mathbf{x}}$ such that for a point $\mathbf{x} \in \Omega$

$$E_{\rm os}(\mathbf{x}) = \exp\left(\lambda\,|\Psi_{\rm os}(\mathbf{x},\mathfrak{a}(\mathbf{x})) - \Psi_{\rm os}(\mathbf{b}_{\mathbf{x}},\mathfrak{a}(\mathbf{b}_{\mathbf{x}}))|\right), \tag{8}$$

where λ is a positive constant. Now we can define a dynamic tensor field $T_{\rm d}:\Omega \to S_2^+$ for $\forall \mathbf{x} \in \Omega$ by

$$T_{\rm d}(\mathbf{x}) := E_{\rm os}(\mathbf{x})\ (T_{\rm os}(\mathbf{x}) + T_{\rm aniso}(\mathbf{x}))\,, \tag{9}$$

where $T_{\rm aniso}$ is defined by

$$T_{\rm aniso}(x) = \mu\,\mathfrak{p}^{\perp}(\mathbf{x}) \otimes \mathfrak{p}^{\perp}(\mathbf{x}), \quad \mu \in \mathbb{R}^+. \tag{10}$$

We set $\mu = 10$ through all the experiments.

IV. Fast Marching Implementation

The fast marching front visits all the grid points in $\mathbb{Z}^2$. It computes the geodesic distances in a monotonically increasing order from the source points, coupled with a course of label assignment [2], [3]. During the geodesic distance computation, each grid point is assigned a label which is either *Far*, *Accepted* or *Trial*. A basic point for the fast marching method is the stencil map $\mathcal{S}$ which defines the neighbourhood for each grid point. In order to deal with the anisotropic case, a complicated metric-dependent stencil construction method should be used [3]. In this paper, we make use of state-of-the-art fast marching method proposed by Mirebeau [3] as our Eikonal solver, where the C++ codes can be downloaded from Anisotropic FM.

At the initialization step, all the source points are tagged as *Trial* while the remaining grid points in $\mathbb{Z}^2$ are tagged as *Far*. In each distance update step, we seek a *Trial* point $\mathbf{x}_{\rm min}$ with the minimal geodesic distance. The point $\mathbf{x}_{\rm min}$ is immediately tagged as *Accepted*, from which one can back track a curve length-parameterized geodesic $\bar{\mathcal{C}}_{\mathbf{x}_{\rm min}}$ joining $\mathbf{x}_{\rm min}$ to the source point, i.e., $\bar{\mathcal{C}}_{\mathbf{x}_{\rm min}}(0) = \mathbf{x}_{\rm min}$. By this geodesic, we can determine two points $\mathbf{a}_{\rm min}$ and $\mathbf{b}_{\rm min}$ can be identified

$$\mathbf{a}_{\rm min} = \bar{\mathcal{C}}_{\mathbf{x}_{\rm min}}(u_1), \quad \mathbf{b}_{\rm min} = \bar{\mathcal{C}}_{\mathbf{x}_{\rm min}}(u_2), \tag{11}$$

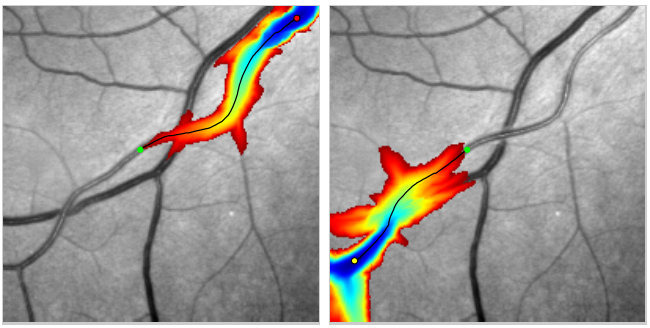

Fig. 3. Partial fronts propagation scheme. The geodesic distance maps superimposed on the retinal patch. The black curves indicate the geodesics for which the endpoints are respectively $\mathbf{s}$ and $\mathbf{q}$.

where u_1, $u_2 \in (0, L_{\mathbf{x}_{\min}})$ with $L_{\mathbf{x}_{\min}}$ the Euclidean curve length of $\bar{\mathcal{C}}_{\mathbf{x}_{\min}}$, and $u_1 \leq u_2$. For each non-accepted[1] neighbour point $\mathbf{x}_{\mathrm{n}} \in \mathcal{S}_*(\mathbf{x}_{\min})$ where $\mathcal{S}_*(\mathbf{x}_{\min}) = \{\mathbf{y} \in \mathbb{Z}^2; \mathbf{x}_{\min} \in \mathcal{S}(\mathbf{y})\}$, we approximate the reference points $\mathbf{a}_{\mathbf{x}_{\mathrm{n}}}$ and $\mathbf{b}_{\mathbf{x}_{\mathrm{n}}}$ by

$$\mathbf{a}_{\mathbf{x}_{\mathrm{n}}} = \mathbf{a}_{\min}, \quad \mathbf{b}_{\mathbf{x}_{\mathrm{n}}} = \mathbf{b}_{\min}.$$

Henceforth we note $\mathbf{a}_{\mathbf{x}_{\mathrm{n}}}$ and $\mathbf{b}_{\mathbf{x}_{\mathrm{n}}}$ as $\mathbf{a}$ and $\mathbf{b}$ for simplicity. Based on the reference points $\mathbf{a}$ and $\mathbf{b}$, we can update the tensors $T_{\mathrm{d}}(\mathbf{x}_{\mathrm{n}})$.

In order to estimate the geodesic distance $\mathcal{U}_{\mathbf{s}}(\cdot)(\mathbf{x})$, we need to solve the following Hopf-Lax operator [3]

$$\mathcal{U}_{\mathbf{s}}(\mathbf{x}) = \min_{\mathbf{y} \in \partial\mathcal{S}(\mathbf{x})} \left\{ \|\mathbf{y} - \mathbf{x}\|_{T_{\mathrm{d}}(\mathbf{x})} + \mathrm{I}_{\mathcal{S}(\mathbf{x})} \mathcal{U}_{\mathbf{s}}(\mathbf{y}) \right\}, \tag{12}$$

where $\mathrm{I}_{\mathcal{S}} \mathcal{U}_{\mathbf{s}}(\mathbf{y})$ is a distance value estimated by the piecewise linear interpolator $\mathrm{I}_{\mathcal{S}(\mathbf{x})}$ in the stencil $\mathcal{S}(\mathbf{x})$.

In contrast to the general fast marching method which starts the front propagation only from the source point $\mathbf{s}$, here we adopt the partial fronts propagation style [20] which starts the propagation simultaneously from the source point $\mathbf{s}$ and the endpoint $\mathbf{q}$. A saddle point $\mathbf{x}^*$ is the *first* meeting point of the two fronts expanding from the respective points $\mathbf{s}$ and $\mathbf{q}$. It can be defined by

$$\mathbf{x}^* = \underset{\mathbf{x}:\ \mathcal{U}_{\mathbf{s}}(\mathbf{x}) = \mathcal{U}_{\mathbf{q}}(\mathbf{x})}{\arg\min} \ \mathcal{U}_{\mathbf{s}}(\mathbf{x}), \tag{13}$$

where $\mathcal{U}_{\mathbf{s}}$ and $\mathcal{U}_{\mathbf{q}}$ are the geodesic distance maps associated to the fixed points $\mathbf{s}$ and $\mathbf{q}$. Based the maps $\mathcal{U}_{\mathbf{s}}$ and $\mathcal{U}_{\mathbf{q}}$, we can define a new geodesic distance map $\mathcal{U}$ by

$$\mathcal{U}(\mathbf{x}) = \min\{\mathcal{U}_{\mathbf{s}}(\mathbf{x}), \mathcal{U}_{\mathbf{q}}(\mathbf{x})\}.$$

The procedure for the dynamic metrics-based partial fronts propagation can be found in Algorithm 1. We illustrate an example for this partial fronts propagation scheme in Fig. 3. Note that the fast marching front propagation will be terminated once the saddle point $\mathbf{x}^*$ is detected.

Note that the idea of using feature coherence penalization to construct dynamic metric during the geodesic distance propagation was also considered in [21]. However, the method developed in this paper mainly differs to [21] in two ways: (i) we take into account a new adaptive anisotropy tensor field T_{aniso} (see Eq. (10)) to enhance the geodesics computation. (ii) the tubular appearance feature is built by the smoothed OS map instead of using the vesselness map[2] itself in [21].

[1] A non-accepted point is a point tagged as *Trial* or *Far*.

Algorithm 1 PARTIAL FRONTS PROPAGATION SCHEME

Output: The distance map $\mathcal{U}$ and the saddle point $\mathbf{x}^*$.

Initialization:

- $\forall \mathbf{x} \in \mathbb{Z}^2 \backslash \{\mathbf{s}, \mathbf{q}\}$, set $\mathcal{U}(\mathbf{x}) \leftarrow \infty$ and set $\mathcal{V}(\mathbf{x}) \leftarrow$ *Far*.
- $\forall \mathbf{x} \in \{\mathbf{s}, \mathbf{q}\}$, set $\mathcal{U}(\mathbf{x}) \leftarrow 0$ and set $\mathcal{V}(\mathbf{x}) \leftarrow$ *Trial*.
- $\forall \mathbf{x} \in \{\mathbf{s}, \mathbf{q}\}$, set $\mathfrak{p}(\mathbf{x}) \leftarrow \arg\max_\theta \Psi_{\mathrm{os}}(\mathbf{x}, \theta)$.

while $\mathbf{x}_{\min}$ is not a saddle point **do**
  Find $\mathbf{x}_{\min}$, the *Trial* point which minimizes $\mathcal{U}$.
  Set $\mathcal{V}(\mathbf{x}_{\min}) \leftarrow$ *Accepted*.
  Find the reference points $\mathbf{a}$ and $\mathbf{b}$.
  for All $\mathbf{x}_{\mathrm{n}} \in S_*(\mathbf{x}_{\min})$ and $\mathcal{V}(\mathbf{x}_{\mathrm{n}}) \neq$ *Accepted* **do**
    Set $\mathcal{V}(\mathbf{x}_{\mathrm{n}}) \leftarrow$ *Trial*.
    UPDATEFRONTDISTANCE$(\mathbf{x}_{\mathrm{n}}, \mathcal{U}, \mathcal{V}, \mathfrak{p}, \mathbf{a}, \mathbf{b})$.
  end for
end while

Algorithm 2 UPDATEFRONTDISTANCE$(\mathbf{x}_{\mathrm{n}}, \mathcal{U}_{\mathbf{s}}, \mathfrak{p}, \mathbf{a}, \mathbf{b})$

Update the feature vector $\mathfrak{p}(\mathbf{x}_{\mathrm{n}})$ by $\mathbf{a}$ via Eq. (7).
Update $T_{\mathrm{d}}(\mathbf{x}_{\mathrm{n}})$ by the reference point $\mathbf{b}$ via Eq. (9).
Estimate the distance value $\mathcal{U}_{\mathrm{tem}}(\mathbf{x}_{\mathrm{n}})$ by evaluating (12).
Set $\mathcal{U}_{\mathbf{s}}(\mathbf{x}_{\mathrm{n}}) \leftarrow \min\{\mathcal{U}_{\mathrm{tem}}(\mathbf{x}_{\mathrm{n}}), \mathcal{U}_{\mathbf{s}}(\mathbf{x}_{\mathrm{n}})\}$.

V. EXPERIMENTAL RESULTS

We compare our model to the anisotropic radius-lifted Riemannian (ARLR) metric [6] and the Finsler elastica (FE) metric [8] on both synthetic and real images.

In Fig. 4, we compare the dynamic metric against the ARLR metric and the FE metric. Our goal is to extract a tubular structure with weak appearance features between the two points which are indicated by dots. Both the geodesics from the ARLR metric (Fig. 4b) and the FE metric (Fig. 4c) favour to pass through the way with stronger appearance, whereas the proposed method is able to delineate the desired structure, which can be seen from Fig. 4d.

In Fig. 5, we illustrate the minimal path extraction results derived from the ARLR metric, the FE metric and the proposed dynamic metric on retinal images, which are shown in columns 1 to 3, respectively. The user given points are indicated by dots. From column 1, we can observe the short branches combination problem suffered by the ARLR metric, where the extracted paths prefer to pass through vessel segments with strong appearance feature. In the first two rows of column 2, we can see the curvature-penalized geodesics pass by wrong vessel segments due to the complicated structures of the vessel network. In the third column, our model can get the desired results thanks to the feature coherence-penalized nature.

[2] The vesselness map is defined as: $\max_r \hat{\rho}(x, r)$.

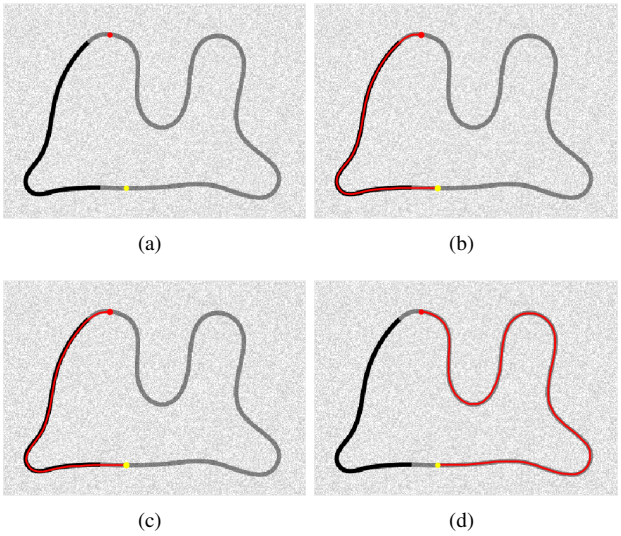

Fig. 4. Comparison results on a synthetic image. **a** A synthetic image which includes a tubular shape. **b-d** Minimal paths obtained via the ARLR metric, the FE metric and the proposed metric. The dots indicate the user-provided points.

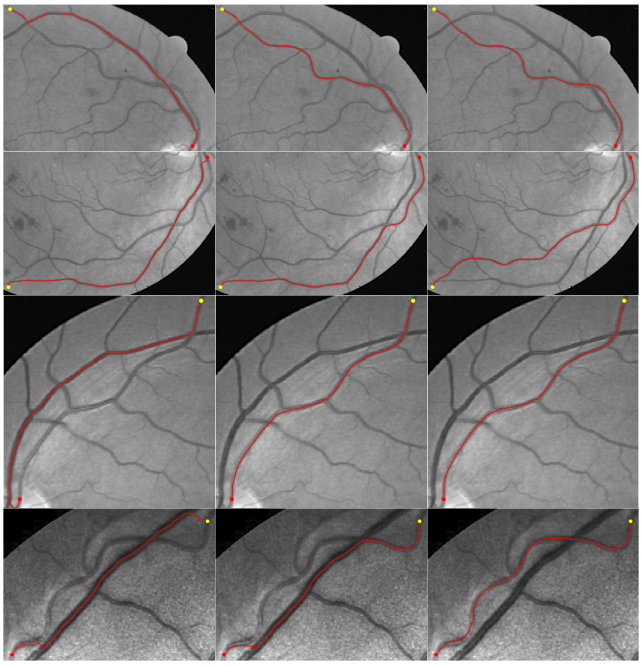

Fig. 5. Comparison results on retinal images. **Columns 1-3** Minimal paths derived from the ARLR metric , the FE metric and the dynamic metric, respectively.

We validate the proposed dynamic minimal path model on 45 retinal patches from the DRIVE dataset [22]. Each patch includes a retinal artery vessel which is near a stronger retinal vein vessel or crosses it. Our goal is to extract the artery vessel between two user-provided points. The artery-vein (A-V) groundtruth for the DRIVE dataset can be found in [23]. Let $\mathbb{A}$ be the set of the grid points inside the desired regions (such as the artery vessels) and let $|\mathbb{A}| \in \mathbb{R}_0^+$ be the number

TABLE I
QUANTITATIVE COMPARISONS OF DIFFERENT METRICS ON DRIVE.

$\mathbb{A}$	Θ	ARLR	FE	Dynamic
A-V Groundtruth	Avg.	0.32	0.66	0.93
	Max.	0.97	1.0	1.0
	Min.	0.02	0.15	0.59
	Std.	0.21	0.29	0.08
Dilated Skeleton	Avg.	0.28	0.51	0.77
	Max.	0.95	0.91	0.95
	Min.	0.02	0.14	0.33
	Std.	0.21	0.24	0.13

of elements of the set $\mathbb{A}$. In addition, we define a set Γ of grid points such that each grid point involved in Γ is passed by a continuous geodesic. Thus, a measure $\Theta \in [0, 1]$ can be simply defined by $\Theta = |\Gamma \cap \mathbb{A}|/|\Gamma|$. For the DRIVE dataset, we provide two ways to construct the set $\mathbb{A}$, where the first way is directly set $\mathbb{A}$ as the artery vessel map which can be identified from the A-V groundtruth. In this case, the measurement Θ evaluates the ability of reducing the risk of short branches combination problem for each geodesic metric. The second way is to skeletonise the artery regions (derived from the A-V groundtruth) via morphological operators. Following that we perform a dilation operation with radius $\hbar = 1$ on the artery vessel skeletons. Finally, the set $\mathbb{A}$ is obtained by identifying all the grid points which simultaneously belong to the dilated regions and the vessel groundtruth regions (including both artery and vein vessels). In this case, the measurement Θ is able to evaluate the alignment between the extracted geodesic and the desired vessel centerlines in a more restrict manner.

VI. CONCLUSION

In this paper, we propose a new dynamic Riemannian metric for geodesic computation with application to tubularity centerline delineation. The dynamic metric can benefit from the tubular appearance feature coherence property and adaptive anisotropy enhancement, by which we can extract a tubular structure with low variations of appearance features from an image with complicated tree structures. The tubular appearance features are estimated using the tool of orientation scores. The proposed dynamic Riemannian metric is constructed during the fast marching front propagation in terms of the respective reference points. The results show that our method indeed outperforms state-of-the-art minimal path methods.

ACKNOWLEDGMENT

The authors would like to thank the reviewers for their suggestions to improve the presentation of this paper. This research has been funded by Roche pharma (project AMD_short) and by a grant from the French Agence Nationale de la Recherche ANR-16-RHUS-0004 (RHU TRT_cSVD).

REFERENCES

[1] L. Cohen and R. Kimmel, "Global minimum for active contour models: A minimal path approach," *IJCV*, vol. 24, no. 1, pp. 57–78, 1997.
[2] J. A. Sethian, "Fast marching methods," *SIAM Review*, vol. 41, no. 2, pp. 199–235, 1999.

[3] J.-M. Mirebeau, "Anisotropic fast-marching on cartesian grids using lattice basis reduction," *SINUM*, vol. 52, no. 4, pp. 1573–1599, 2014.

[4] G. Peyré, M. Péchaud, R. Keriven, and L. D. Cohen, "Geodesic methods in computer vision and graphics," *Foundations and Trends in Computer Graphics and Vision*, vol. 5, no. 3–4, pp. 197–397, 2010.

[5] H. Li and A. Yezzi, "Vessels as 4-D curves: Global minimal 4-D paths to extract 3-D tubular surfaces and centerlines," *TMI*, vol. 26, no. 9, pp. 1213–1223, 2007.

[6] F. Benmansour and L. Cohen, "Tubular structure segmentation based on minimal path method and anisotropic enhancement," *IJCV*, vol. 92, no. 2, pp. 192–210, 2011.

[7] M. Péchaud, R. Keriven, and G. Peyré, "Extraction of tubular structures over an orientation domain," in *CVPR*, 2009, pp. 336–342.

[8] D. Chen, J.-M. Mirebeau, and L. Cohen, "Global minimum for a Finsler elastica minimal path approach," *IJCV*, vol. 122, no. 3, pp. 458–483, 2017.

[9] E. J. Bekkers *et al.*, "A PDE approach to data-driven sub-Riemannian geodesics in SE (2)," *SIIMS*, vol. 8, no. 4, pp. 2740–2770, 2015.

[10] R. Duits, S. P. Meesters, J.-M. Mirebeau, and J. M. Portegies, "Optimal paths for variants of the 2D and 3D Reeds-Shepp car with applications in image analysis," *to appear JMIV, 2018*, 2016.

[11] W. Liao, S. Worz, C.-K. Kang *et al.*, "Progressive minimal path method for segmentation of 2D and 3D line structures," *TPAMI*, 2017.

[12] F. Benmansour and L. Cohen, "Fast object segmentation by growing minimal paths from a single point on 2D or 3D images," *JMIV*, vol. 33, no. 2, pp. 209–221, 2009.

[13] H. Li, A. Yezzi, and L. Cohen, "3D multi-branch tubular surface and centerline extraction with 4D iterative key points," in *MICCAI*, 2009, pp. 1042–1050.

[14] D. Chen, J.-M. Mirebeau, and L. Cohen, "Vessel tree extraction using radius-lifted keypoints searching scheme and anisotropic fast marching method," *JACT*, vol. 10, no. 4, pp. 224–234, 2016.

[15] J. Ulen, P. Strandmark, and F. Kahl, "Shortest paths with higher-order regularization," *TPAMI*, vol. 37, no. 12, pp. 2588–2600, 2015.

[16] Y. Chen *et al.*, "Curve-like structure extraction using minimal path propagation with backtracking," *TIP*, vol. 25, no. 2, pp. 988–1003, 2016.

[17] M. W. Law and A. C. Chung, "Three dimensional curvilinear structure detection using optimally oriented flux," in *Proceedings of ECCV*, 2008, pp. 368–382.

[18] A. F. Frangi *et al.*, "Multiscale vessel enhancement filtering," in *Proceedings of MICCAI*, 1998, pp. 130–137.

[19] B. Franceschiello, A. Sarti, and G. Citti, "A Neuromathematical model for geometrical optical illusions," *JMIV*, vol. 60, no. 1, pp. 94–108, 2018.

[20] T. Deschamps and L. Cohen, "Fast extraction of minimal paths in 3D images and applications to virtual endoscopy," *MedIA*, vol. 5, no. 4, pp. 281–299, 2001.

[21] D. Chen and L. D. Cohen, "Interactive retinal vessel centreline extraction and boundary delineation using anisotropic fast marching and intensities consistency," in *EMBC*, 2015, pp. 4347–4350.

[22] J. Staal *et al.*, "Ridge-based vessel segmentation in color images of the retina," *TMI*, vol. 23, no. 4, pp. 501–509, 2004.

[23] Q. Hu *et al.*, "Automated separation of binary overlapping trees in low-contrast color retinal images," in *MICCAI*, 2013, pp. 436–443.